Origins of Heavy Precipitation Biases in the TRMM PR and TMI Products Assessed with *CloudSat* and Reanalysis Data

ANDUNG BAYU SEKARANOM[a]

Graduate School of Environmental Studies, Nagoya University, Furo-cho Chikusa-ku, Nagoya, Japan

HIROHIKO MASUNAGA

Institute for Space-Earth Environmental Research, Nagoya University, Furo-cho Chikusa-ku, Nagoya, Japan

(Manuscript received 15 January 2018, in final form 7 November 2018)

ABSTRACT

This study aims to characterize the background physical processes in the development of those heavy precipitation clouds that contribute to the Tropical Rainfall Measuring Mission (TRMM) active and passive sensor differences. The combined global observation data from TRMM, *CloudSat*, and European Centre for Medium-Range Weather Forecasts (ECMWF) interim reanalysis (ERA-Interim) from 2006 to 2014 were utilized to address this issue. Heavy rainfall events were extracted from the top 10% of the rain events from the Precipitation Radar (PR) and TRMM Microwave Imager (TMI) rain-rate climatology. Composite analyses of *CloudSat* and ERA-Interim were conducted to identify the detailed cloud structures and the background environmental conditions. Over tropical land, TMI tends to preferentially detect deep isolated precipitation clouds for relatively drier and unstable environments, while PR identifies more organized systems. Over the tropical ocean, TMI identifies heavy rainfall events with notable convective organization and clear regional gradients between the western and eastern Pacific Ocean, while PR fails to capture the eastward shallowing of convective systems. The PR–TMI differences for the moist and stable environments are reversed over tropical land.

1. Introduction

Precipitation estimates derived from satellite observations are now widely used in various studies related to meteorology and climatology. One of the earliest precipitation estimation methods was developed by using infrared (IR) sensors obtained from geostationary satellites (Griffith et al. 1978). IR sensors measure cloud-top temperatures as a proxy of surface precipitation estimations, although these measurements are known to serve as indirect estimations. Currently, precipitation estimations using passive microwave (PMW) radiometers are widely used, and many satellites carry these instruments. PMW radiometers use a more direct approach of measuring emission signals from liquid-phase hydrometeor contents as well as scattering signals from ice-phase hydrometeors inside precipitating clouds (Wilheit 1986; Wilheit et al. 1994). A further breakthrough was brought about by the Tropical Rainfall Measuring Mission (TRMM) (Kummerow et al. 1998). The TRMM was equipped with a Precipitation Radar (PR) to be used as its active sensor in addition to the TRMM Microwave Imager (TMI), which acted as the passive sensor (Kummerow et al. 1998; Simpson et al. 1996).

Various studies have attempted to explore the origins of the rain-rate differences between PR and TMI (Masunaga et al. 2002; Yamamoto et al. 2008; Zagrodnik and Jiang 2013; Liu and Zipser 2014; Henderson et al. 2017), but only a few studies were focused on the extreme events (Sekaranom and Masunaga 2017), which have a close relationship with disasters. The estimation of the heavy rain rates from satellites remains challenging because of the large uncertainties involved in the estimation process. From a PR point of view, rain

Denotes content that is immediately available upon publication as open access.

[a] Additional affiliation: Faculty of Geography, Gadjah Mada University, Yogyakarta, Indonesia.

Corresponding author: Andung Bayu Sekaranom, andungbayu@geo.ugm.ac.id

DOI: 10.1175/JAMC-D-18-0011.1

rates are determined by the relationships between radar reflectivity Z and rain rate, and between the specific attenuation k and the received reflectivity Z (Iguchi et al. 2000). The Z of the PR sensor within the Rayleigh limit is a product of the sixth moment of the drop size distribution (DSD), which is written as follows:

$$Z = \int_0^\infty N(D) D^6 \, dD, \tag{1}$$

where $N(D)$ is the particle size distribution as a function of diameter D (Heymsfield et al. 2002). The above DSD–reflectivity relationship of the 13.8-GHz radar frequency is subject to considerable attenuation when large raindrops are present, as is typical for heavy rainfall events. To correct attenuation, a hybrid method involving the Hitschfeld–Bordan and surface reference technique is utilized (Iguchi et al. 2000, 2009). Previous studies have found that precipitation estimation biases derived from the PR arise from the assumptions in the DSD and attenuation correction (Iguchi et al. 2009; Kozu et al. 2009; Schumacher and Houze 2000). Some ground validations indicate that the PR often shows rain-rate values that underestimate the heavy rain rates (Henderson et al. 2017; Kirstetter et al. 2013; Zagrodnik and Jiang 2013), especially for convective rains (Iguchi et al. 2009). Rasmussen et al. (2013) pointed out that these differences in extremes over land are likely to be related to mixed-phase and/or frozen hydrometers.

In contrast to PR, TMI uses a physical-based assumption to derive the relationship between the brightness temperature and rain rate (T_B–R). In the standard TMI algorithm, TMI utilizes a Bayesian approach to calculate the probability of the rain rate by comparing the retrieved and observed microwave signals using a hydrometeor profile database (Kummerow and Giglio 1994; Kummerow et al. 2001). Low-frequency T_B values of the TMI results are less sensitive to the DSD assumptions than those from the PR (Masunaga et al. 2002). However, TMI has its own uncertainties when characterizing the ice-phase hydrometeors from the 85-GHz channel (Shige et al. 2004; Zagrodnik and Jiang 2013). Moreover, unlike PR, TMI cannot measure vertical rain structures and, therefore, depends entirely upon assumed vertical cloud structures (Kummerow et al. 2001). TMI has another disadvantage when estimating rain rate over land surfaces because of the noise generated by surface emissions. Therefore, over land surfaces, the TMI algorithm depends entirely on the 85-GHz channel (Wang et al. 2009). Another significant issue of the TMI algorithm is related to its general underestimation trend due to the beamfilling effect (Kummerow 1998; Kummerow et al. 2004). Since TMI has a coarser resolution than PR, especially for the emission channels, biases due to deep isolated precipitation systems can be more significant than they would be for PR (Liu and Zipser 2014). Last, although TMI T_B does not strongly depend on DSD, biases could be generated by the conversion of the liquid water contents to rain rates from the DSD assumption (Masunaga et al. 2002).

Previous works have demonstrated that the biases between PR and TMI rain estimation are influenced by the design and performance of retrieval algorithms. Over land, Zagrodnik and Jiang (2013) showed that TMI has an issue with higher rain-rate retrieval. Petković and Kummerow (2017) found that the frequency of occurrence for specific rainfall regimes containing different profiles of ice particles was essential for describing TMI–PR rainfall differences. The TMI estimation depends mostly on 85-GHz channels over land, which is more sensitive to ice particles (Gopalan et al. 2010; Liu and Zipser 2014). The TMI land algorithm in general estimates higher rainfall associated with higher ice-scattering signals, while PR is not affected by such constraints (Sekaranom and Masunaga 2017). Over the ocean, the discrepancies between the two rain retrievals are largely associated with the precipitation homogeneity (Kummerow 1998; Liu and Zipser 2014; Carr et al. 2015) and convective–stratiform variability within the TMI–PR footprint (Kirstetter et al. 2015; Carr et al. 2015). The TMI is less sensitive to inhomogeneous rain because of coarse-resolution channels (63 km × 37 km at 10 GHz) (Kummerow et al. 1998), which makes TMI estimates biased to heavier rain from larger precipitation systems (Liu and Zipser 2014; Carr et al. 2015). Henderson et al. (2017) showed that TMI tends to produce a higher estimation for the organized stratiform rain and a lower estimation for the deep-isolated convective rain than those of PR. Further, Henderson et al. (2018) found that the central and west Pacific basins TMI–PR differences were related to regional changes in the level of precipitation organization due to ENSO variability. This might be associated with increasing stratiform fraction during El Niño events (Schumacher and Houze 2006).

Masunaga et al. (2002) identified that the differences between PR and TMI are associated with different DSD assumptions. The different DSD assumption, however, also depends on whether the precipitation is classified as convective or stratiform (Iguchi et al. 2000). In general, the proportion of convective and stratiform rains are influenced by their precipitation organization and its corresponding thermodynamics environment. Excessive moisture at the lower to midtroposphere could produce convective outbreaks over a large area (Sherwood 1999; Lucas et al. 2000). Higher humidity also could be produced by the convective feedback, which moistens the surrounding environment and makes favorable to future

convection (Tompkins 2001). Those sustaining convective systems, in general, could be associated with largely organized systems with considerable stratiform components. In contrast to the precipitation systems developed in a moister environment, smaller precipitation systems tend to be developed at a dryer environment (Schumacher and Houze 2006; Hill and Lackmann 2009). The small precipitation systems could also be associated with isolated convective cells (Schumacher and Houze 2003), which contain no or fewer stratiform components than the largely organized systems. It is therefore useful to characterize the PR–TMI heavy rain estimation biases in term of precipitation organization and its corresponding thermodynamics environment.

Using previous studies involving the PR and TMI comparisons and validations (Berg et al. 2006; Furuzawa and Nakamura 2005; Shige et al. 2006), we can characterize the differences of the PR and TMI results, particularly for heavy rain events. It has been shown by Sekaranom and Masunaga (2017) that over some tropical land areas, PR tends to detect heavy rain rates with lower storm-top heights (STH) better than TMI at any given rain rate. Furthermore, the corresponding reflectivity profiles show a significant increase below the melting layer compared to that of TMI. These findings suggest that PR detects extreme warm rain events with significant collision and coalescence processes near the surface (Hamada et al. 2015; Song and Sohn 2015). Hamada et al. (2015) and Song et al. (2017) showed that the rain with lower STH identified by PR is associated with a more humid but more stable environment. Song et al. (2017) further argued that the extreme events identified by PR could occur in a more stable environment since the higher humidity enhances the graupel production in the midtroposphere. The above differences are less significant over the ocean than over the land. Sekaranom and Masunaga (2017) showed that the differences of the STH as a function of rain rate over the ocean are not as distinct as those over land. However, studies by Liu and Zipser (2014) showed that TMI identifies greater precipitation areas than PR over the global ocean. From the above studies, we could infer that these extreme biases are related to the amounts of ice particles at aloft and/or the scale of precipitation systems and convective variability that might be not clearly identified from the climatological biases.

Although previous results characterized well the PR–TMI uses for estimating rain rates, the reasons for why the different preferences exist were left unresolved. This study aims to assess the origins of the biases, particularly for heavy rain events. Identifying the origin of the heavy rain biases could help in developing more accurate satellite estimations, which are useful in disaster early-warning systems and understanding the future climate. To address this issue, the corresponding cloud structures from *CloudSat* and the background environmental profiles from ERA-Interim are utilized. *CloudSat* provides information about cloud droplets, which are not captured by PR. The utilization of *CloudSat* in this research gives more detailed background analysis to explain the origin of the biases.

The description of the datasets and explanations of the research methodology are shown in detail in section 2. The PR–TMI differences when estimating heavy rainfall events are shown in section 3. The differences are further examined using the *CloudSat* cloud structures accompanying the PR–TMI differences and are shown in section 4. The corresponding environmental profiles are shown in section 5. The discussion of the differences in the physical processes and their relationships with convective structure organizations are shown in section 6.

2. Methodology

a. Dataset

This study utilizes the TRMM precipitation data from PR and TMI as the core dataset for the comparative analysis. The 94-GHz radar reflectivity data from *CloudSat* are used to explain the different cloud structures associated with the PR and TMI heavy rainfall events. Several environmental variables from ERA-Interim were used to explain the thermodynamic environments involved in the formation of PR and TMI heavy rainfall events. The detailed information for each dataset is shown in Table 1.

The TRMM product used in this research is the version 7 level 2 product. The level 2 product contains the instantaneous precipitation data from TRMM PR and TMI. The PR precipitation dataset analyzed in this work was obtained from the near-surface rain rates from the TRMM PR 2A25 product (NASA 2011c). This product has an approximately 5 km $\times$ 5 km horizontal resolution at nadir and a 250-km swath width (Iguchi et al. 2000; Kummerow et al. 1998). The TMI precipitation dataset was obtained from the TRMM TMI 2A12 product (NASA 2011b). The horizontal resolution is coarser than that of PR but has a broader swath width than PR ($\pm$900 km) (Kummerow et al. 1998). The TMI surface flags from the same product are used to classify the surface types and separate the study area into ocean and land surfaces. To further examine the details of the differences originating from the emission and ice-scattering patterns obtained by the PMW sensor, the brightness temperature dataset from TRMM TMI 1B11 is also analyzed (NASA 2011a).

TABLE 1. Data description.

Platform	Instrument	Description	Resolution	Target parameters
TRMM	PR	13.8-GHz radar	4.3 km (at nadir)	Near-surface rain rate (2A25), corrected radar reflectivity (2A25)
TRMM	TMI	Passive microwave imager	Varies from 7 km × 5 km (85 GHz) to 63 km × 37 km (10 GHz)	Near-surface rain rate (2A12), brightness temperatures (1B11)
CloudSat	CPR	94-GHz radar	1.4 km × 1.7 km	Radar reflectivity
ERA-Interim	—	ECMWF Re-Analysis	Gridded 0.75°	Air temperature, specific humidity, relative humidity, and vertical velocity profiles

The cloud properties corresponding to the PR and TMI heavy rainfall events are derived from *CloudSat*, which has operated from 2006 until present. *CloudSat* carries a 94-GHz Cloud Profiling Radar (CPR) that captures the vertical cloud profiles (Stephens et al. 2002; Austin et al. 2009). By design, the CPR measurements provide only cross-section profiles of the clouds below its track with a horizontal resolution of approximately 1.4 km × 1.7 km. This resolution is approximately 3 times finer than that of TRMM PR. In this analysis, the CPR reflectivity data from the *CloudSat* level 2B Geometrical Profile product (2B-GEOPROF) are used (CloudSat DPC 2017). Cloud flag data stored in the same product are also obtained to classify the cloud and noncloud states. The rain-type data from the *CloudSat* 2C Precipitation Column product (2C-PRECIP-COLUMN) are also analyzed to classify the observed rain events into convective and stratiform precipitation events. The *CloudSat* measurements are matched in space and time with the TRMM.

The ERA-Interim data contain atmospheric reanalysis products with a horizontal grid resolution of approximately 0.75° × 0.75° and contain 37 vertical levels, spanning from 1000 to 1 hPa (Dee et al. 2011). The ERA-Interim dataset is available for 1979 to the present (ECMWF 2017), which covers the TRMM and *CloudSat* observational periods. The data are available for 4 times a day. In this analysis, the air temperature, specific humidity, relative humidity, and vertical velocity data are used to explain the physical processes corresponding to the PR–TMI differences.

b. Data preprocessing

The global tropical areas are divided into several domains to identify the regional differences in the PR and TMI estimations of extreme rain events. The regions are further classified into ocean and land subregions. Over the tropical ocean, the domains are divided into the 1) global tropical ocean (GlobalTropics; 15°S–15°N, 180°–180°), 2) Maritime Continent (MaritimeCont; 15°S–15°N, 90°–150°E), 3) tropical west Pacific (WestPac; 15°S–15°N, 150°E–180°), 4) tropical central Pacific (CentralPac; 15°S–15°N, 130°W–180°), and 5) tropical east Pacific (EastPac; 15°S–15°N, 90°–130°W). Over the tropical land, the domains were divided into the 1) global tropical land (GlobalTropics; 15°S–15°N, 180°–180°), 2) Maritime Continent (MaritimeCont; 15°S–15°N, 90°–150°E), 3) South America (SouthAm; 35°S–15°N, 45°–80°W), and 4) central Africa (CentralAf; 15°S–15°N, 15°–45°E). The domains are shown in Fig. 1. The analysis spans 2006–14, when TRMM, *CloudSat*, and ERA-Interim data are available.

First, the precipitation data from PR and TMI are plotted onto a 0.25° × 0.25°-resolution grid, following Sekaranom and Masunaga (2017). All sample data points (raining and nonraining pixels) inside each grid point are averaged to represent the gridpoint rain-rate value. This process ensures that the influences of the differences of the original PR and TMI resolutions when capturing precipitation are minimized. A heavy rainfall event database is then constructed by taking the uppermost 10% of the grid rain rates by using rain-rate distribution defined in each region. The uppermost 10% thresholds for each region are shown in Table 2. Using the 10% threshold as an extreme criterion rather than using an even higher threshold ensures that the combined datasets capture sufficient observations. The database contains information about the grid rain rate, the grid center coordinate, the maximum rain rate inside the grid, the geolocations of the maximum rain rates inside the grid, and the recording times of each identified heavy rainfall event.

The TMI brightness temperature data are also gridded following the same rules as the PR and TMI precipitation data. Over the ocean surface, the brightness temperature data from all nine TMI channels are analyzed. Only the brightness temperature data from the 85-GHz vertical and horizontal polarization channels are used for the land surfaces. The ocean and land surfaces are also determined using the TMI surface flag at the 0.25° × 0.25° grid resolution. If more than two-thirds of the grid is dominated by ocean flags, the grid is classified as an ocean grid. A similar criterion was used for

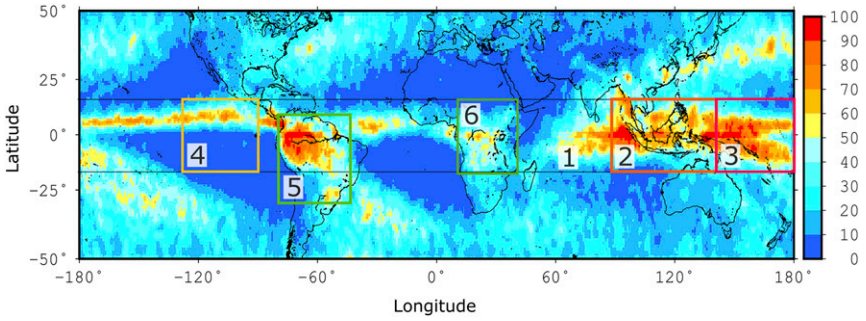

FIG. 1. Regional domains in this analysis. Shaded colors show the number of *CloudSat* deep convective cases over 1) the global tropics, 2) the Maritime Continent, 3) the west Pacific, 4) the east Pacific, 5) South America, and (6) central Africa.

the land grids. Grids that did not fulfill the above conditions were not considered in this analysis.

The combination of TRMM-*CloudSat* data are achieved by using a similar method to that described by Masunaga (2012). In this analysis, the precipitation events identified by the TRMM are utilized as the coordinates and time centers to be matched with the *CloudSat* data. Utilizing the temporal differences between the TRMM and *CloudSat* data, the precipitation cloud properties before, at, and after extreme events are reconstructed. Although the temporal changes could be easily obtained, identifying the heavy precipitation clouds at a 0.25° × 0.25° resolution could produce inaccurate results since *CloudSat* has a very narrow field of view (FOV). Therefore, only slices of the TRMM gridded data that overlap with the *CloudSat* FOV (1.4 km × 1.7 km) are considered. The coordinates with the maximum rain rates inside each TRMM grid are utilized to ensure that *CloudSat* captures the center of the heavy precipitation systems. Only grids where the *CloudSat* coordinates are centered between −5 and +5 km from the coordinate of the TRMM maximum rain rate are selected. In addition, *CloudSat* cross sections that occupy less than 80% of the length of each grid (≈15 *CloudSat* profiles within each grid) are removed. The maximum time difference between the TRMM and *CloudSat* observations is set to ±1.5 h. These strict criteria limit the number of samples from *CloudSat* to about 80 samples over the land domains (Table 3). The 1.5-h time window is selected because narrower time lags (20, 40, and 60 min) have been found to show consistent results among each other except for and enhanced statistical noise owing to the reduced sample size.

Two-dimensional (horizontal distance–height) composite cloud fractions are constructed to diagnose the PR and TMI extreme precipitation cloud structures. The composite cloud fractions are generated by using a similar method to that described by Igel et al. (2014). In the first step, clouds are identified using the minimum detected reflectivity threshold of −28 dB*Z*. The corresponding heavy precipitating clouds are identified by iteratively classifying contiguous adjacent cloud pixels surrounding the cloud pixels located at the nearest distance to the TRMM maximum rain inside each grid. The iteration process will classify contiguous cloud pixels as a single cloud. Therefore, only the single cloud closest to the coordinate of the maximum rain rate inside each grid point is considered when building the composite cloud fractions. Each single cloud from a set of observations are stacked together into composite cloud structure to represent the cloud vertical and horizontal extents. Although the precipitating systems have various sizes and shapes associated with them (e.g., Nesbitt et al. 2006), the composite of the heavy precipitating clouds are considered to statistically represent the ''average'' cloud structure. The minimum number of cloud composite is about eight observations over the Maritime Continent land and higher for other regions, so the composite structure is unlikely to be distorted by a single, exceptional event.

To further explain the PR and TMI extreme precipitation cloud differences, the convective and stratiform cloud fractions are calculated using the *CloudSat* rain-type flags. The convective:stratiform ratios are

TABLE 2. The uppermost 10% rain-rate thresholds to determine extreme rain events at each domain.

Region	Ocean		Land	
	PR	TMI	PR	TMI
GlobalTropics	10.86	9.16	11.78	12.42
MaritimeCont	11.43	9.31	11.39	10.81
WestPac	10.95	9.18	—	—
EastPac	10.55	9.38	—	—
SouthAm	—	—	11.79	11.11
CentralAf	—	—	12.27	13.68

calculated for each 1.5-h bin for the 6 h before and after the heavy rain rates were identified by the TRMM.

In contrast to the TRMM instantaneous rain rates, the ERA-Interim dataset has 6-h observation intervals and coarser resolutions than the gridded precipitation database. In this analysis, those ERA-Interim grid coordinates nearest to the corresponding TRMM grid are obtained to represent the environmental profiles. Only the ERA-Interim data that fall between 1.5 h before and after the TRMM extreme events are considered. The potential temperature and specific humidity profiles are then averaged for each ocean and land region. The convective available potential energy (CAPE) is calculated to explain the relationship between the PR–TMI extreme rain rates with environmental instability:

$$\mathrm{CAPE} = \int_{\mathrm{LFC}}^{\mathrm{EL}} g\left[\frac{\theta(z) - \overline{\theta_v}(z)}{\overline{\theta_v}(z)}\right] dz,$$

where LFC is the level of free convection, EL is the height of the equilibrium level (neutral buoyancy), $\theta(z)$ is the virtual potential temperature of the specific parcel, $\overline{\theta_v}(z)$ is the virtual potential temperature of the environment, and g is the acceleration due to gravity. The CAPE was averaged for each 1.5-h bin from 24 h before and after the extreme events observed in the TRMM, similarly to the method described by Masunaga (2012).

3. TRMM PR and TMI differences

In this section, the observed differences between the PR and TMI when identifying heavy precipitation events are demonstrated. First, the joint distribution plots of the collocated TMI 85-GHz minimum polarization corrected brightness temperatures (PCTs) versus the rain rates are shown. The 85-GHz PCTs could be utilized as a proxy of the amount of ice particles near the cloud top. Lower 85-GHz PCTs indicate the existence of abundant ice particles from the observed rain event. The 85-GHz PCTs were calculated using the T_B differences between the vertical T_{BV} and horizontal polarizations T_{BH}, following Zagrodnik and Jiang (2013), where $\mathrm{PCT} = 1.818T_{BV} - 0.818T_{BH}$.

Plots of the probability distribution functions (PDFs) of the collocated TMI brightness temperatures corresponding to the PR and TMI uppermost 10% rain rates are also compared in this section. Over the ocean domains, the PDF plots for the 10-, 19-, 21-, 37-, and 85-GHz brightness temperature data are presented. Over the land domains, only the 85-GHz brightness temperature data are shown. The plots of the collocated TMI 85-GHz minimum PCTs versus the rain rates over each ocean area are shown in Fig. 2. This figure indicates that both PR and TMI show a broad relationship between the near-surface rain and the collocated 85-GHz PCTs. The broad relationship indicates that heavy rain occurrence do not strictly associated with the amount of ice particles. A similar result was obtained by Sekaranom and Masunaga (2017) over the Maritime Continent. The figure also shows that for TMI, the upper-end distributions of extreme events are found at higher PCTs compared to PR. In Fig. 2, the white lines pinpoint the PCT where the maximum number of events are observed for rain rates above the uppermost 10%. The TMI lines correspond to slightly higher PCTs at some regions compared to PR. This indicates that TMI estimates heavy rain events with fewer ice particles than identified by PR.

TABLE 3. Total number of observed *CloudSat*-collocated profiles for the TRMM rain rate greater than the uppermost 10%.

Region	Ocean		Land	
	PR	TMI	PR	TMI
GlobalTropics	2092	1703	730	940
MaritimeCont	457	396	103	80
WestPac	339	268	—	—
EastPac	175	174	—	—
SouthAm	—	—	432	491
CentralAf	—	—	176	220

The plots of the collocated TMI 85-GHz minimum PCTs versus the rain rates over the land domains are shown in Fig. 3. This figure shows the clear contrast between PR and TMI. The PR joint distribution plots show similar relationships for the ocean domains. In contrast to PR, TMI shows a strong relationship between the two parameters. This strong relationship is expected since the TMI land algorithm has a "built in" linear relationship between the rain rates and 85-GHz T_B values (Sekaranom and Masunaga 2017). As a result, TMI tends to detect higher numbers of events at lower PCTs (about 160–180 K above the uppermost 10% rain events, as shown via the white lines in Fig. 3). This confirms that heavy rain events identified by TMI over land are accompanied by a large amount of ice particles. Extreme rain events identified by PR, on the other hand, do not directly depend on the amount of ice particles similarly to over ocean.

The PDF plots of the collocated TMI 85-GHz brightness temperatures for the PR and TMI extreme events over the ocean domains are shown in Fig. 4. This figure shows that the TMI exhibits a contrast between the Maritime Continent to the eastern Pacific Ocean. The Maritime Continent is characterized by warmer sea surface temperatures (SST) because of its position between the Pacific and the Indian Ocean warm pools (Ramage 1968). The PR extreme events tend to have lower 10-GHz brightness temperatures than the TMI extremes over the

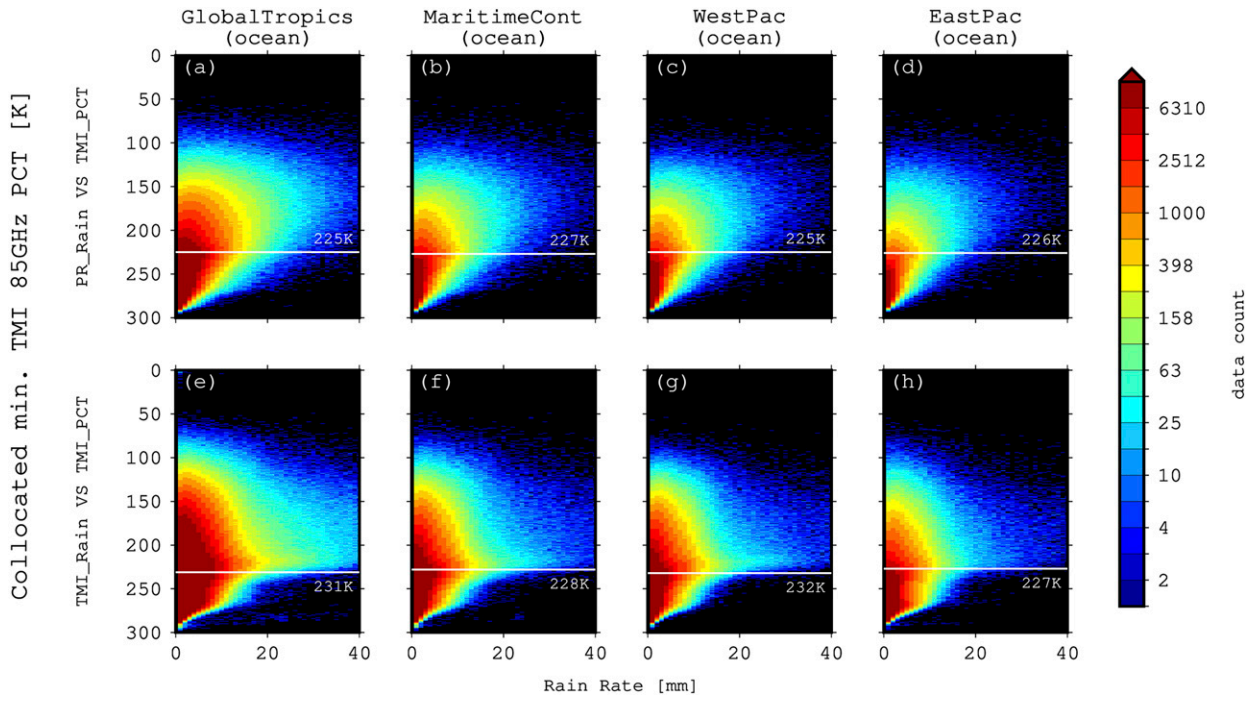

FIG. 2. Joint distribution of collocated minima TMI 85-GHz PCTs vs (a)–(d) PR rain rates and (e)–(h) TMI rain rates for ocean regions. (left to right) Global tropics, Maritime Continent, west Pacific, and east Pacific. The color bar indicates the number of data points. The white lines indicate the brightness temperature where the rain frequency above the uppermost 10% reached a maximum.

Maritime Continent. The TMI extreme events produce slightly lower brightness temperatures at 85-GHz than the PR extreme events over the Maritime Continent. This contrasts with the eastern Pacific Ocean, where the TMI extreme events have higher brightness temperatures at 85-GHz than the PR extremes. The brightness temperature contrast indicates that TMI identifies more heavy rain events with abundant ice particles over the Maritime Continent than PR identifies, and the opposite is true over the east Pacific Ocean.

The plots of the collocated TMI 85-GHz brightness temperature PDFs for the PR and TMI extreme events over the land domains are shown in Fig. 5. All the regions show that the TMI extreme events are characterized by lower brightness temperatures than the PR extreme events at the rightmost edge of the distribution, while the TMI PDF is skewed slightly warmer than the PR PDF. The difference in skewness indicates that TMI tends to identify more rain events associated with abundant ice particles over all the land domains than PR identifies because of the tight assumption of rain rates and ice particles in the TMI land algorithm.

4. *CloudSat* heavy precipitation cloud structure differences

A comparison between the PR and TMI datasets suggests that the active and passive TRMM sensors are systematically different in their methods of identifying heavy precipitation events. Further analysis focused on the detailed cloud structures would be beneficial for explaining the PR–TMI extreme precipitation event differences. In this section, the differences between the PR–TMI extreme events are compared by utilizing the *CloudSat* observations. The composite cloud fractions and convective and stratiform cloud fractions from *CloudSat* are examined next. Last, the PR–TMI differences in identifying heavy rain events are examined in terms of the convective organizations. Since many variables could be utilized to characterize this organization (Rickenbach and Rutledge 1998), in this research, the organizations are simply defined with regard to the horizontal scales of the systems. The more organized systems are associated with larger cloud structures and vice versa. This assumption is supported by *CloudSat* observation from different time windows that shows that the horizontal cloud extents are continuously increasing after the convective peaks are reached.

The *CloudSat* cloud fractions associated with the PR and TMI extremes over the ocean domains are shown in Fig. 6. TMI displays regional variations from the Maritime Continent to the eastern Pacific Ocean. Over the Maritime Continent, the TMI extreme events correspond to taller and horizontally extensive clouds.

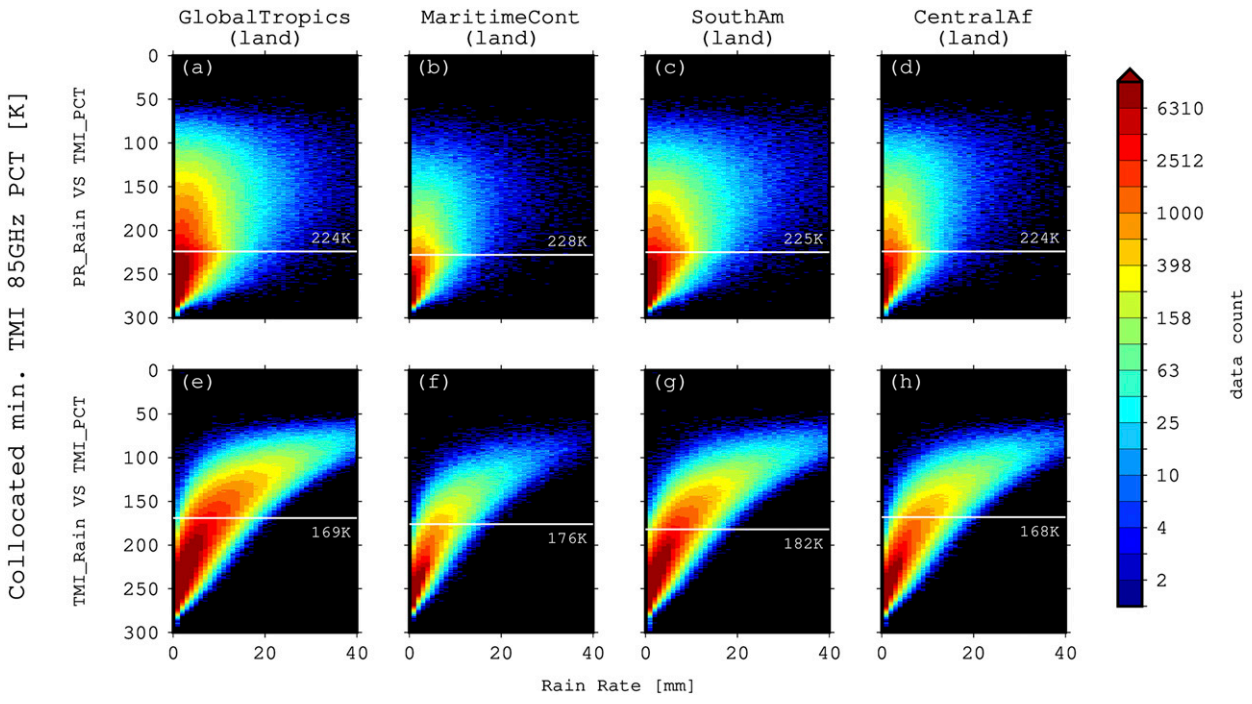

FIG. 3. As in Fig. 2, but for the land domains.

However, the heights continuously decrease toward the eastern Pacific Ocean. Over the eastern Pacific Ocean, the TMI tends to identify shallow clouds. (Liu and Zipser 2013) showed that shallow–wide clouds are predominant in this area. TMI somehow detects these clouds as extremes rather than detecting the taller clouds identified by PR. Moreover, the differences among the ocean regions identified by PR do not display this gradual change. Shige et al. (2008) showed that PR captures the contrast between the western and eastern Pacific Oceans that mainly occur during La Niña. In the present results, the PR rainfall over the eastern Pacific Ocean produces a similar profile to that of the western Pacific Ocean, possibly because this work exclusively targeted extreme events.

The corresponding PR and TMI extreme precipitation cloud fractions over the land domains are shown in Fig. 7. The *CloudSat* cloud fractions over the land domains differ from those over the ocean domains. All land domains show that the TMI extreme events are confined to narrow convective cells. In contrast, the PR extreme events are generated by more horizontally extensive cells with lower cloud-top heights than those of TMI. Sekaranom and Masunaga (2017) showed that the PR extremes with relatively low STHs could generate greater rain rates ($>30\,\mathrm{mm\,h^{-1}}$) than the TMI extremes with taller STHs.

Yamamoto et al. (2008) found a time lag between the peaks of the convective rainfall events detected by PR and TMI. This implies that the PR and TMI detect different stages of convection. In this research, the *CloudSat* convective and stratiform fractions were used to characterize the degrees of convective organization. The *CloudSat* convective and stratiform fractions corresponding to the PR and TMI extreme events over the ocean and the land domains are shown in Fig. 8. A different feature is observed between the Maritime Continent and the eastern Pacific Ocean. Over the Maritime Continent, an earlier convective peak is identified by TMI, occurring approximately 3 h before the extremes detected by the TRMM, while the PR convective peak occurs 1.5 h before. Liu and Zipser (2014) showed that TMI tends to detect greater precipitation areas than PR. The greater precipitation areas could be generated by more horizontally extensive cells with earlier convective peaks than those detected by PR.

From the above results, we can characterize the PR–TMI differences in terms of the convective organizations. The degree of organization of the systems also can be characterized based on the time differences between the peaks. Over the Maritime Continent ocean, TMI captures more organized systems than PR. This result is reversed over the eastern Pacific Ocean, where TMI captures less organized systems than PR. Over land, the PR in general captures more organized systems than TMI. Over the Maritime Continent land, the less organized systems identified by TMI are associated with a

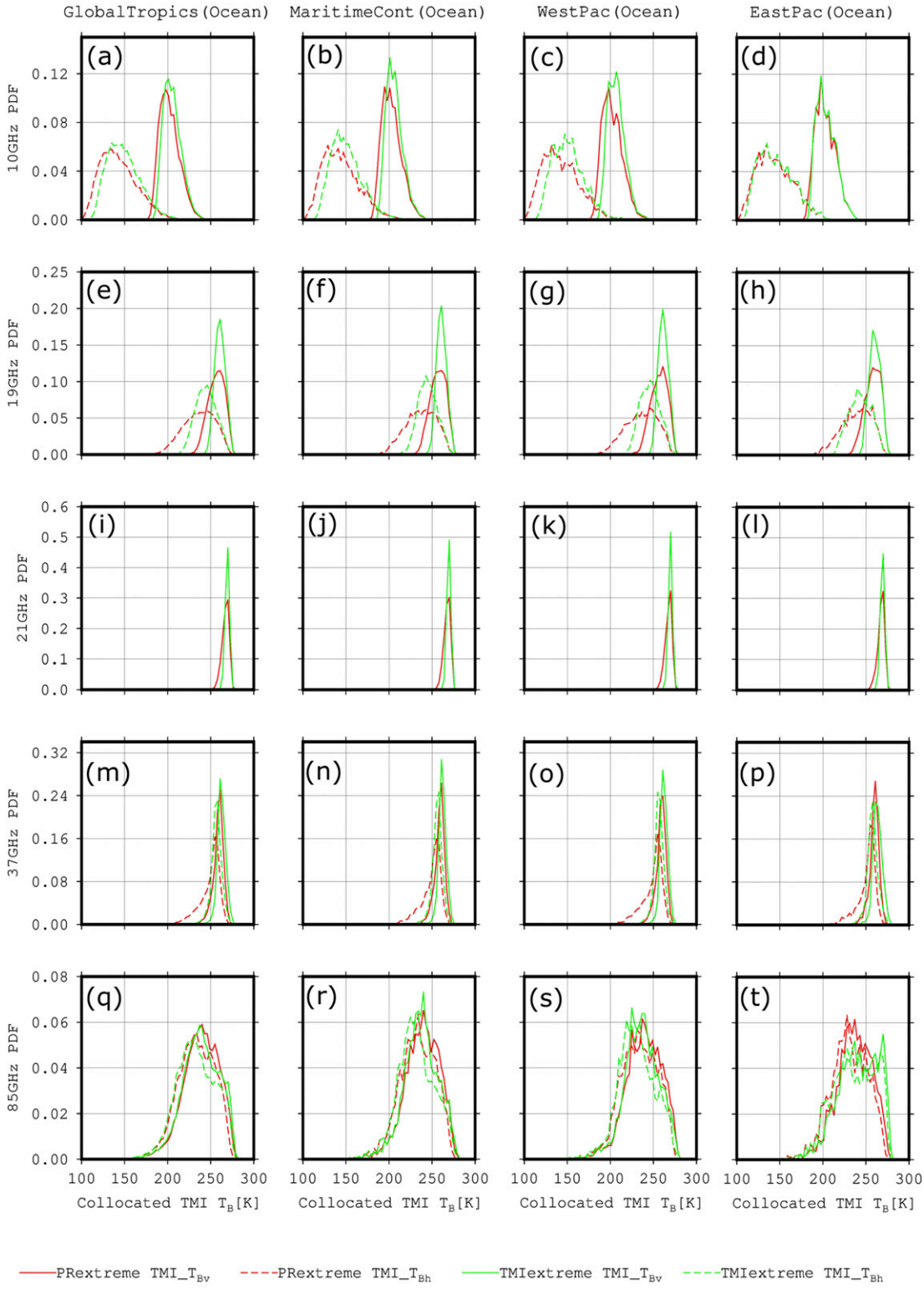

FIG. 4. Collocated TMI brightness temperatures for the PR and TMI extreme events over the oceans for (left to right) each region and (top to bottom) the brightness temperature channels.

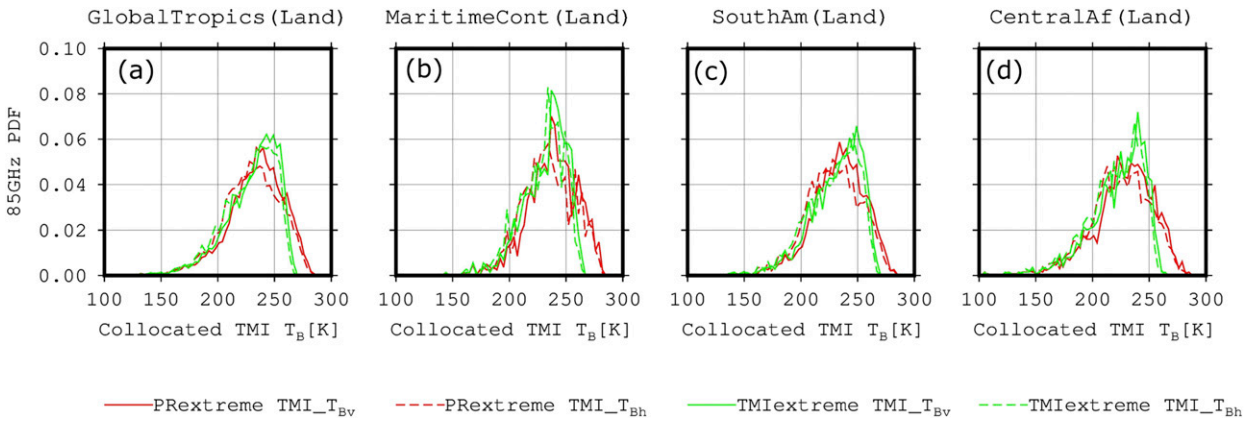

FIG. 5. As in Fig. 4, but for the land domains.

later convective peak than PR, whereas over South America and central Africa, the less organized precipitation systems identified by TMI are associated with a larger convective fraction (Figs. 8g,h).

5. Influence of environmental conditions on the PR–TMI rain-rate estimation differences

To further study the physical processes in the precipitation cloud development, comparisons of the environmental profiles from ERA-Interim are given in this section. First, the potential temperature and humidity profile differences corresponding to the PR and TMI extreme events are compared. The influence of the instabilities in the PR and TMI heavy precipitation cloud development is further explained using the corresponding CAPE.

The corresponding PR–TMI environmental profile differences over the ocean domains are shown in Fig. 9. The results show that the TMI extreme events occurred

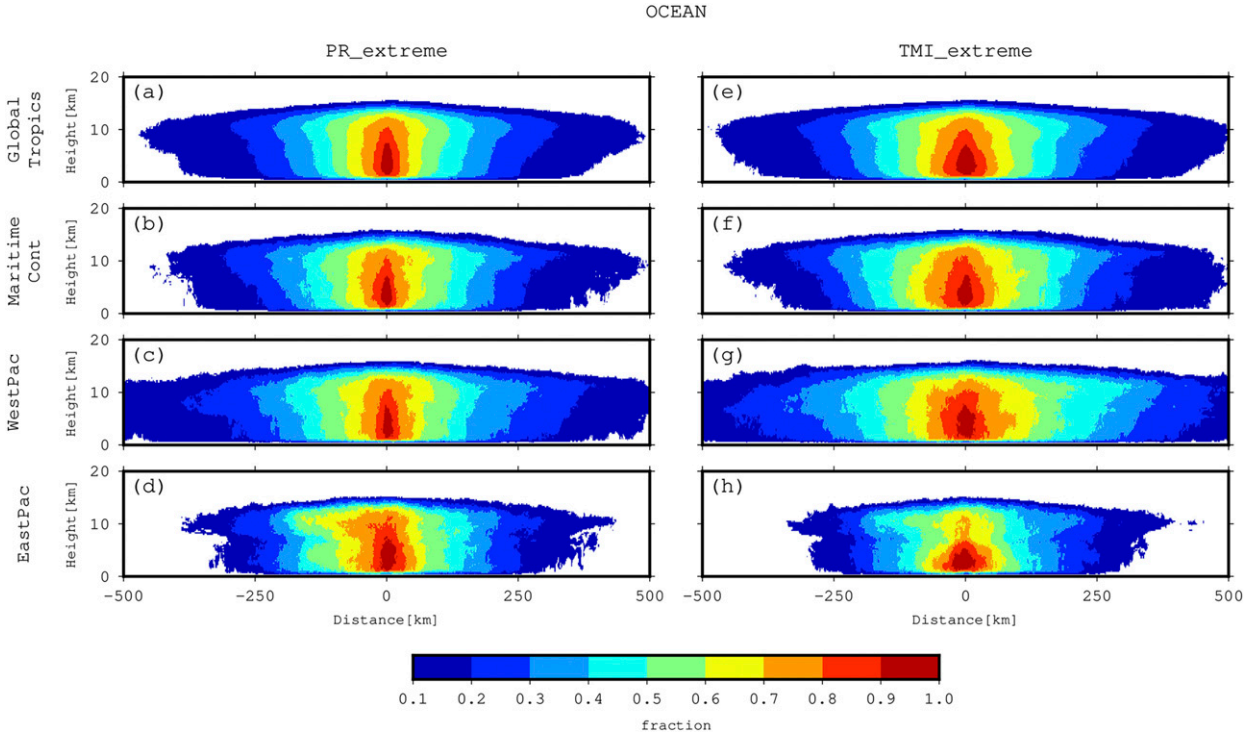

FIG. 6. *CloudSat* collocated cloud fractions for the (a)–(d) PR extreme events and (e)–(h) TMI extreme events over the examined ocean domains. (a),(e) Global tropical ocean, (b),(f) Maritime Continent, (c),(g) west Pacific, and (d),(h) east Pacific.

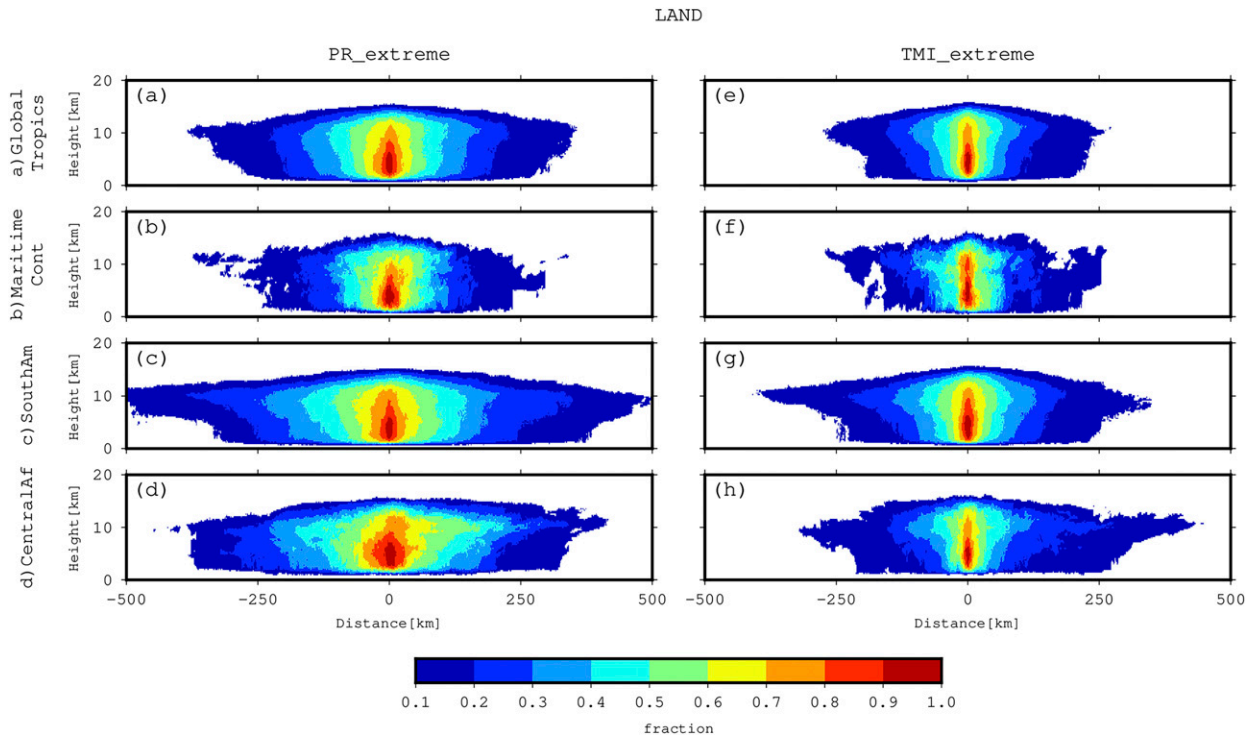

FIG. 7. As in Fig. 6, but for the land domains. (a),(e) Global tropical land, (b),(f) Maritime Continent, (c),(g) South America, and (d),(h) central Africa.

in more humid environments than those of PR. A contrast is also observed from the Maritime Continent compared to the eastern Pacific Ocean. Lower heights at which the humidity difference is largest are observed over east Pacific Ocean compared to the Maritime Continent ocean. Over the Maritime Continent and west Pacific Ocean, the TMI extreme events correspond to higher humidities throughout the troposphere. Over the eastern Pacific Ocean, the humidity excesses for the TMI extremes are reversed and become humidity deficits above 500 hPa and near the surface.

The PR extreme events over the ocean domains generally have slightly warmer potential temperatures near the surface, but have colder values above the 500-hPa level than those of the TMI extreme events. The Maritime Continent–eastern Pacific Ocean contrast is also present in the potential temperature profiles. As identified by PR, the Maritime Continent is characterized by lower potential temperatures in the midtroposphere and shows only slight differences from the TMI values near the surface. Over the eastern Pacific Ocean, the near-surface temperature differences become larger.

The corresponding PR–TMI environmental profile differences over the land domains are shown in Fig. 10. This figure shows that the PR extreme events occur at higher specific humidities than the TMI extreme events for all identified regions, except near the surface, which differs from the results for the ocean extremes. Higher specific humidities were observed, especially at the 850–500-hPa level. Furthermore, the corresponding PR extreme events show colder potential temperatures near the surface than those of the TMI extreme events. The greater humidity but lower potential temperature differences corresponding to the PR extreme events were also identified by Hamada et al. (2015) and Song and Sohn (2015). However, the ocean has considerably different thermodynamic characteristics than those of the land domains, and clouds cannot be explained by the above results.

To examine the possible temporal change of the above environmental profile differences, temporal plots of the specific humidity and potential temperature over the global tropical land and ocean are shown in Fig. 11. The figure shows that over land, a deepening of the lower-tropospheric cold bias and a rapid development of dry bias toward the time of the precipitation occurrence are observed in association with the TMI extremes compared to the PR extremes. The overall patterns are nevertheless qualitatively similar to what has been seen at $t = 0$ (Figs. 9 and 10). Over ocean, the temporal changes are even less significant compared to the land environmental profiles.

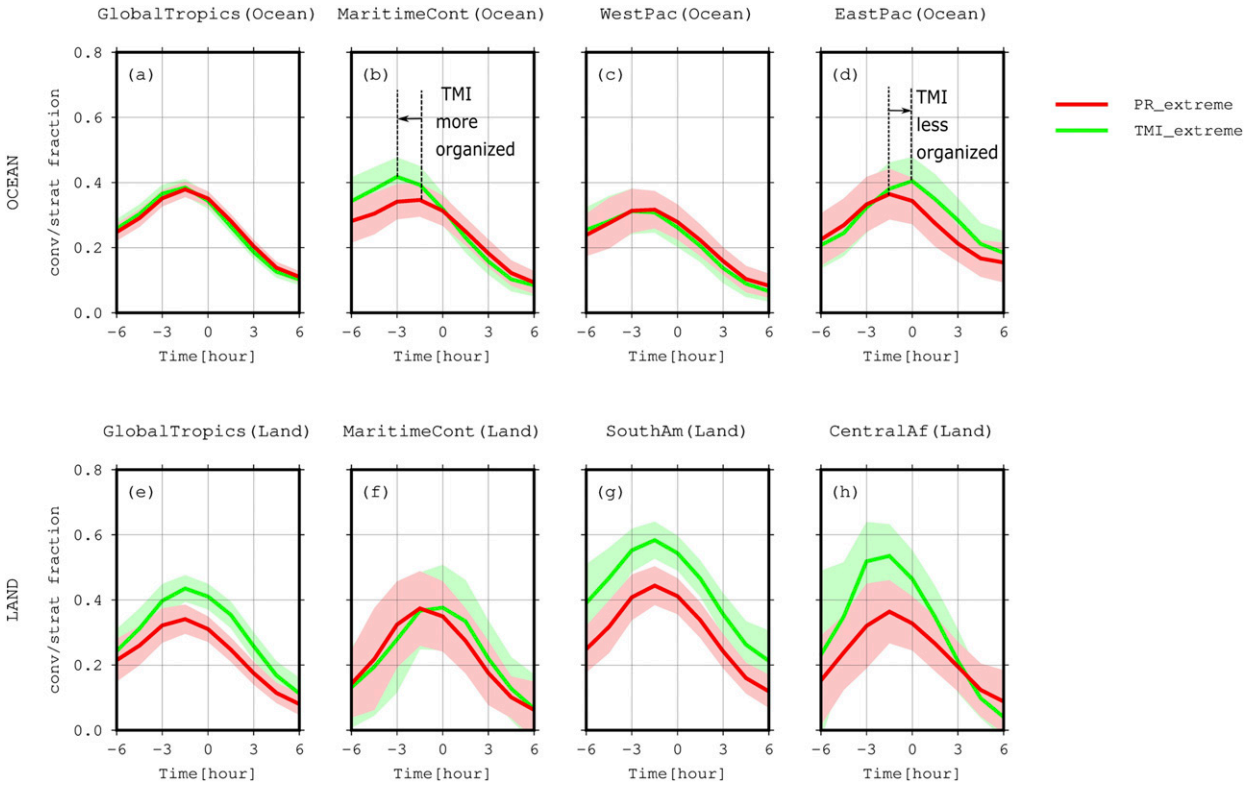

FIG. 8. *CloudSat* convective fractions for the PR extreme events (red line) and TMI extreme events (green line) over the (a)–(d) ocean and (e)–(h) land. The shaded color represents the 95% confidence interval.

The CAPE plots corresponding to the PR and TMI extreme events over the ocean and land domains are shown in Fig. 12. In general, the highest rain rates are detected with downward slopes after the CAPE drops following a maximum that resembles tropical deep convective clouds (Masunaga 2012). In general, the PR extreme events over the ocean domains have higher CAPE values than the TMI extreme events. The ocean

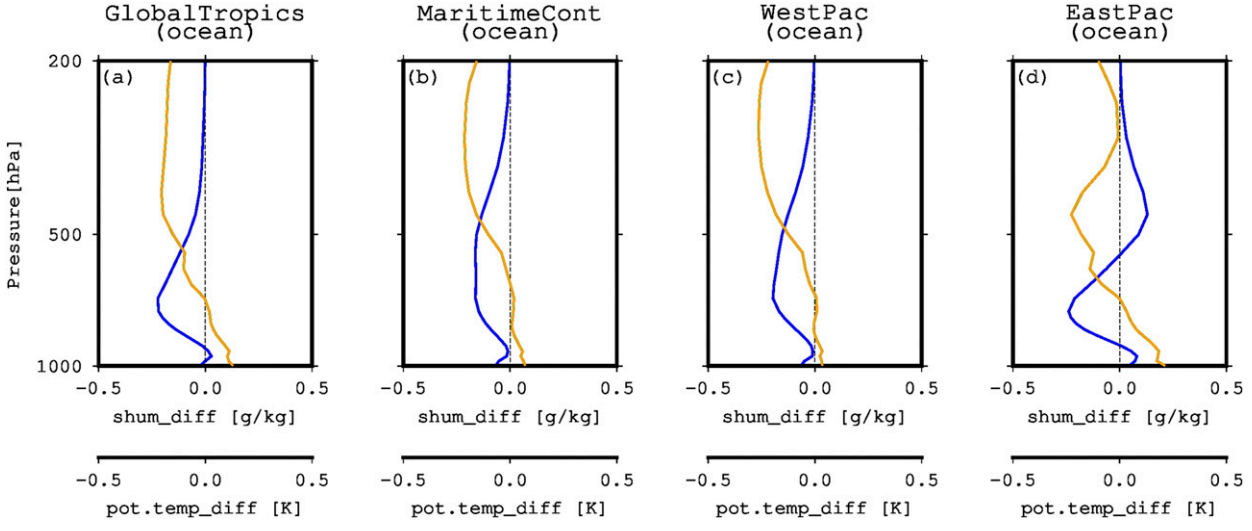

FIG. 9. Potential temperature anomalies (pot.temp_diff; orange) and specific humidity anomalies (shum_diff; blue) from the ERA-Interim over ocean regions in terms of the PR–TMI differences.

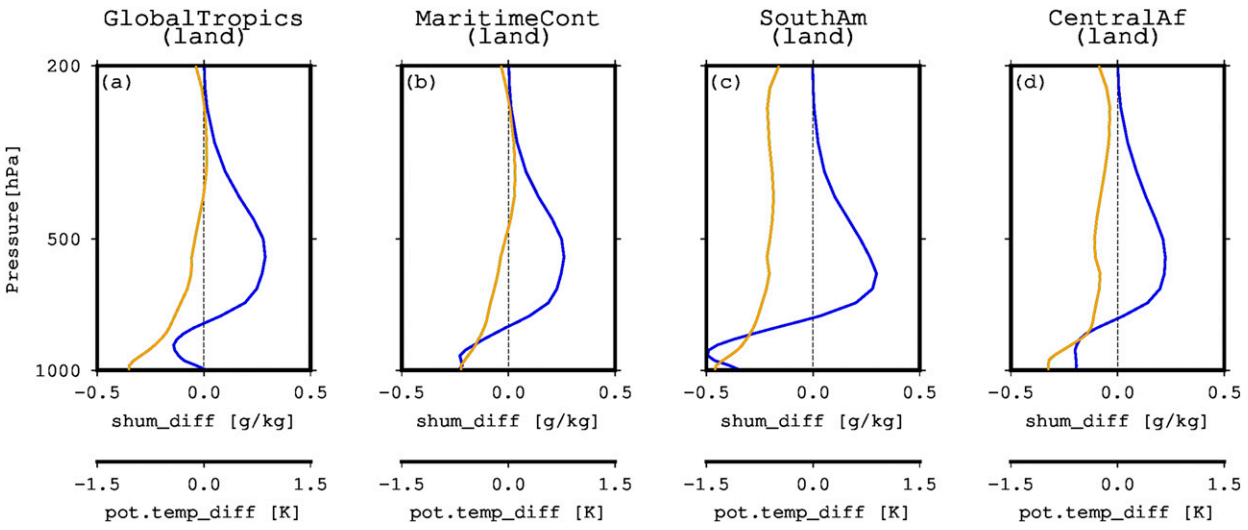

FIG. 10. As in Fig. 9, but for the land domains.

CAPEs are also higher for the western Pacific compared to the eastern Pacific, with the CAPE reaching a maximum over the Maritime Continent. TMI extremes prefer slightly more stable environments than the PR extremes as implied by the potential temperature profiles shown earlier.

Over the land domains, the corresponding TMI CAPEs are greater than the PR CAPEs with notable diurnal variations. This result indicates that the TMI extreme events occur in more unstable environments than the PR extreme events, differing from the ocean composite. Regional differences of the CAPE in Fig. 12 show that heavy rain events over the Maritime Continent (land) and central Africa in general are generated by higher CAPE than over South America. Lower CAPE might be associated with precipitation that is generated by the more oceanic environment over South America (Masunaga et al. 2002; Sekaranom and Masunaga 2017). Extreme rain events with high CAPE are identified over central Africa, which is often associated with strong afternoon heating (Liu and Zipser 2005). The strong instability is possibly related to the higher rain rates estimated by TMI than PR for the general rain events (Liu and Zipser 2014). However, for extreme rain events, the PR captures some events that are associated with a more stable environment than identified by TMI.

6. Discussion and conclusions

This study investigates the precipitation biases from the TRMM active–passive sensors due to cloud and environmental properties. The combination of the TRMM, *CloudSat*, and ERA-Interim data provides comprehensive information to explain the PR–TMI estimation differences. The general properties of the PR–TMI differences in identifying the heavy rainfall events are further discussed in this section.

Noticeable differences between the PR and TMI extreme events are observed over the land domain. The clear ice-scattering signatures (Fig. 3) and horizontally confined cloud structures (Fig. 7) of the TMI extremes indicate that the TMI heavy rain events are associated with isolated deep convective clouds over land (Fig. 13b, right). Plots from the ERA-Interim data show that the TMI extreme events over land occur in drier free-troposphere conditions but in more unstable environment than the PR extreme events. The CAPE patterns (Fig. 12) also indicate that the diurnal forcing strongly controls the heavy rain events, primarily via afternoon surface heating (Yamamoto et al. 2008). The more unstable environment produces higher cloud tops and can produce more abundant ice particles aloft (Song et al. 2017), which can then produce a stronger ice-scattering signal.

In contrast to the deep isolated clouds identified by the TMI, the PR extremes over land tend to be associated with more organized systems (Fig. 13b, left). The absence of a strong relation between the PR rain rates and the TMI 85-GHz PCTs (Fig. 3) implies that the PR extremes are not always associated with a substantial amount of ice-phase hydrometeors aloft (Furuzawa and Nakamura 2005; Sekaranom and Masunaga 2017). The extreme precipitation clouds corresponding to the PR extreme events show more horizontally extensive convective cells than those associated with the TMI heavy rainfall events (Fig. 7). The PR heavy rainfall events are associated with moister environments in the free troposphere as well as

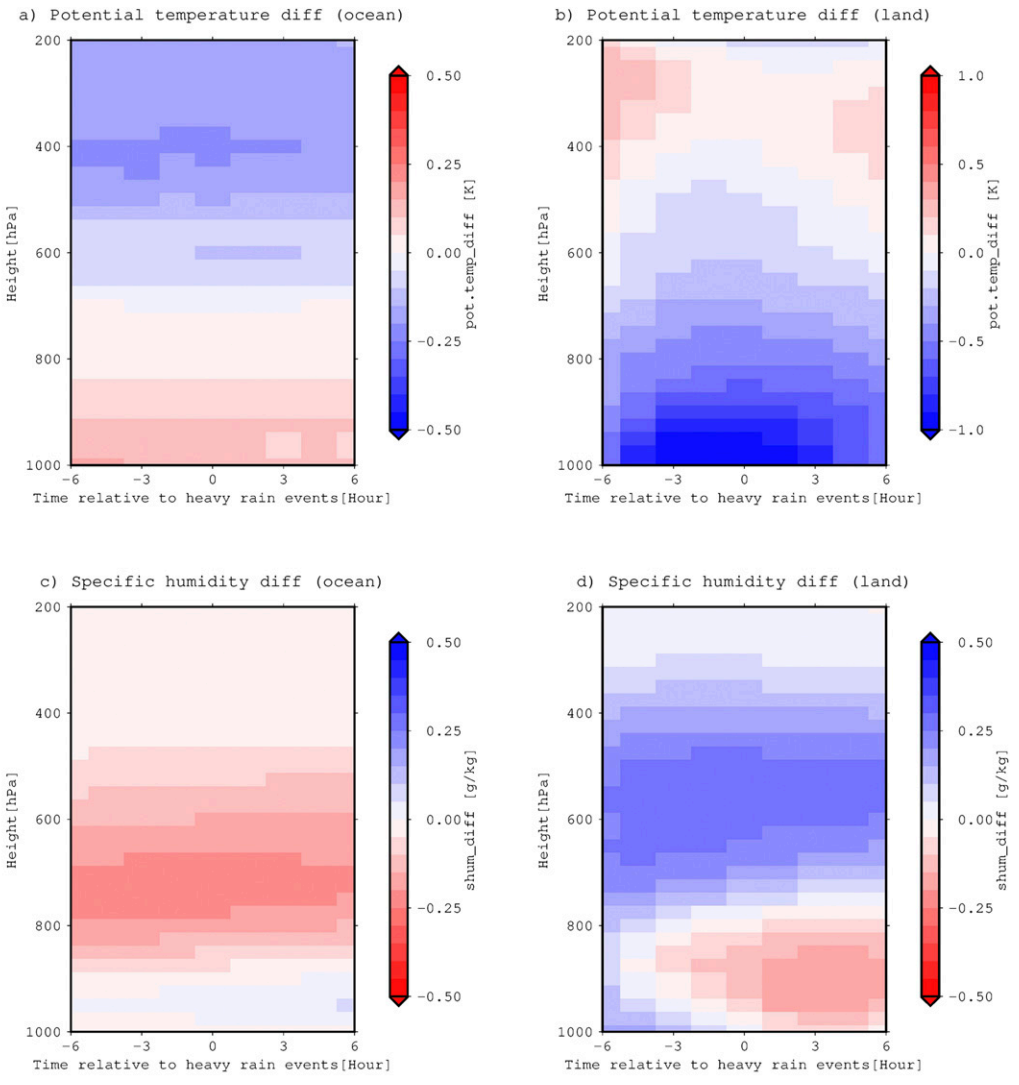

FIG. 11. Temporal changes of the potential temperature anomalies and specific humidity anomalies from the ERA-Interim before and after heavy rain events identified by the TRMM. The plots are for global tropical (a),(c) ocean and (b),(d) land in terms of the PR–TMI differences.

more stable environments than the TMI heavy rainfall events (Fig. 12). This more stable environment produces lower cloud-top heights and less confined cloud structures, which include warm rain extremes (Song et al. 2017). These warm rain extremes may be missed by TMI because of the lack of ice particles.

The TMI extremes are not essentially different from the PR extremes over ocean domains in terms of their PCTs (Fig. 2). However, the collocated TMI microwave emissions indicate regional differences of TMI over the ocean domains (Fig. 4) that also differ from the PR extreme events. Over the eastern Pacific Ocean, the collocated *CloudSat* cloud-top heights corresponding to the TMI extreme events are lower than those of the PR extreme events (Fig. 6). It appears that their horizontal extent is much larger than those of individual cumulus clouds (Liu and Zipser 2013), although it is smaller than found in other oceanic regions. (Fig. 13a, bottom right). The shallow horizontally extensive clouds are associated with moister environments near the surface but drier environments than those of their PR counterparts at approximately the 500-hPa level (Fig. 9). The shallow horizontally extensive clouds were also found in a more stable environment than that identified by PR (Fig. 12). In contrast to the shallow horizontally extensive clouds, the higher cloud-top heights associated with the PR heavy rainfall events correspond to more unstable environments.

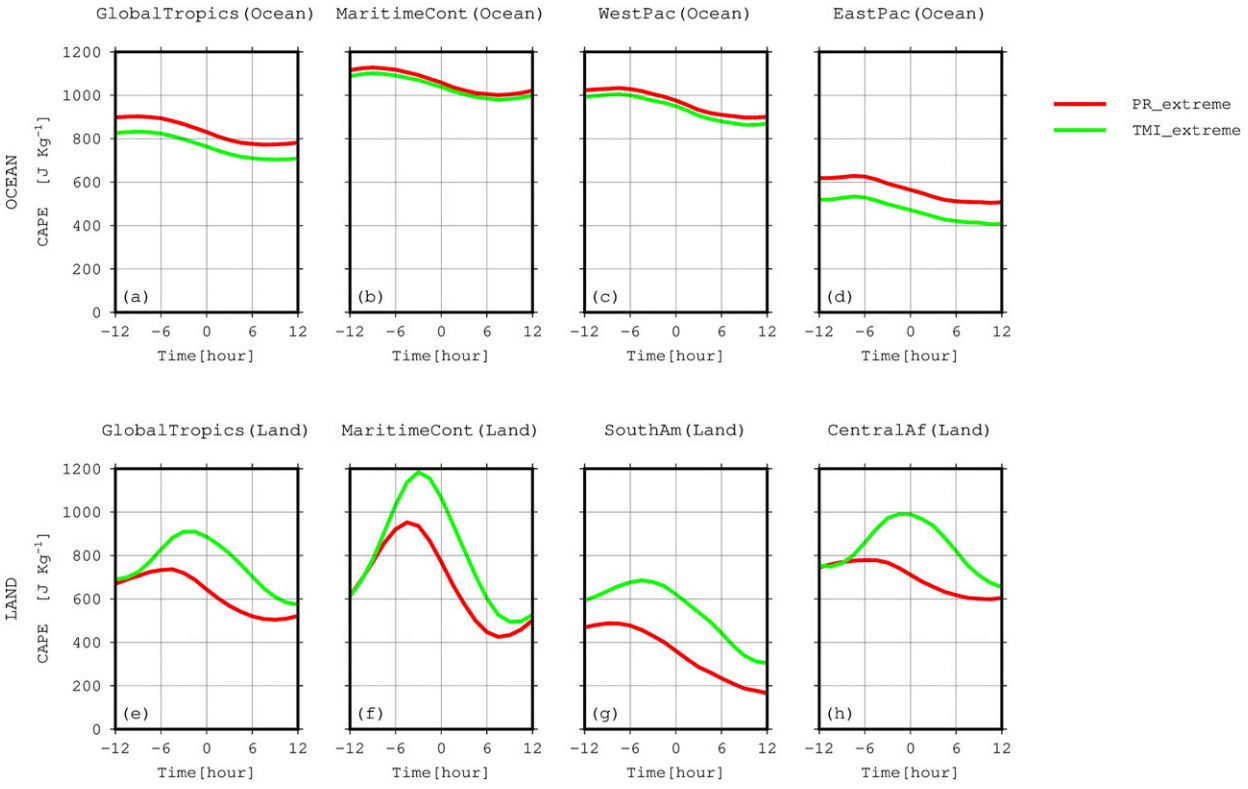

FIG. 12. Temporal changes of the collocated CAPE from the ERA-Interim data for the PR extreme events (red) and TMI extreme events (green).

Comparisons among the ocean domains show a regional transition of the extreme precipitation cloud structures from the eastern to western parts of the Pacific Ocean. Over the western Pacific Ocean, the *CloudSat* profiles show that the horizontal extents are slightly broader for the TMI extremes than for the PR heavy rainfall events (Fig. 6). The TMI convective fraction is greater, and its peak occurs earlier than the PR convective peak, which implies that TMI detects heavily organized precipitation systems (Fig. 13a, top right). Based on the corresponding environmental conditions, the TMI extreme events tend to occur in more humid and stable environments than the PR extreme events (Fig. 12). In the case of TMI extreme events, the moister environment (Fig. 9) could produce more extensive convective cloud systems. The moister environment could be partially due to rain evaporation in stratiform clouds, which moistens the atmosphere.

A comparison over the ocean domain suggests that the beamfilling effect (Kummerow 1998) has a strong influence on the TMI heavy rain-rate estimation. Over both the eastern and western Pacific Oceans, TMI captures horizontally extensive clouds despite the cloud-top heights being lower over the eastern Pacific Ocean. This result suggests that TMI tends to detect larger precipitation areas than PR, as identified by Liu and Zipser (2014). Furthermore, the result shows that this strong emission might be associated with higher stratiform fractions. As identified by Henderson et al. (2017), TMI tends to estimate higher rain rates for stratiform rain than PR.

This paper attempts to explain the differences between the TRMM PR and TMI when identifying heavy rainfall events over the global tropical lands and oceans. The results show that PR and TMI detect heavy rainfall events from distinct physical processes that can be explained in terms of precipitation organization. Characterizing this organization could provide a potential application for reducing the biases between the PR and TMI rain-rate estimations. The results presented in this paper also represent a potential contribution to improving satellite precipitation estimations and their derived products when active–passive satellite sensors are combined.

The future works of this research will focus on whether different degrees of precipitation organization could be utilized to reduce the rain estimation biases between the PR and TMI and on whether the bias pattern as a function of organization is consistent over time, particularly across different ENSO phases.

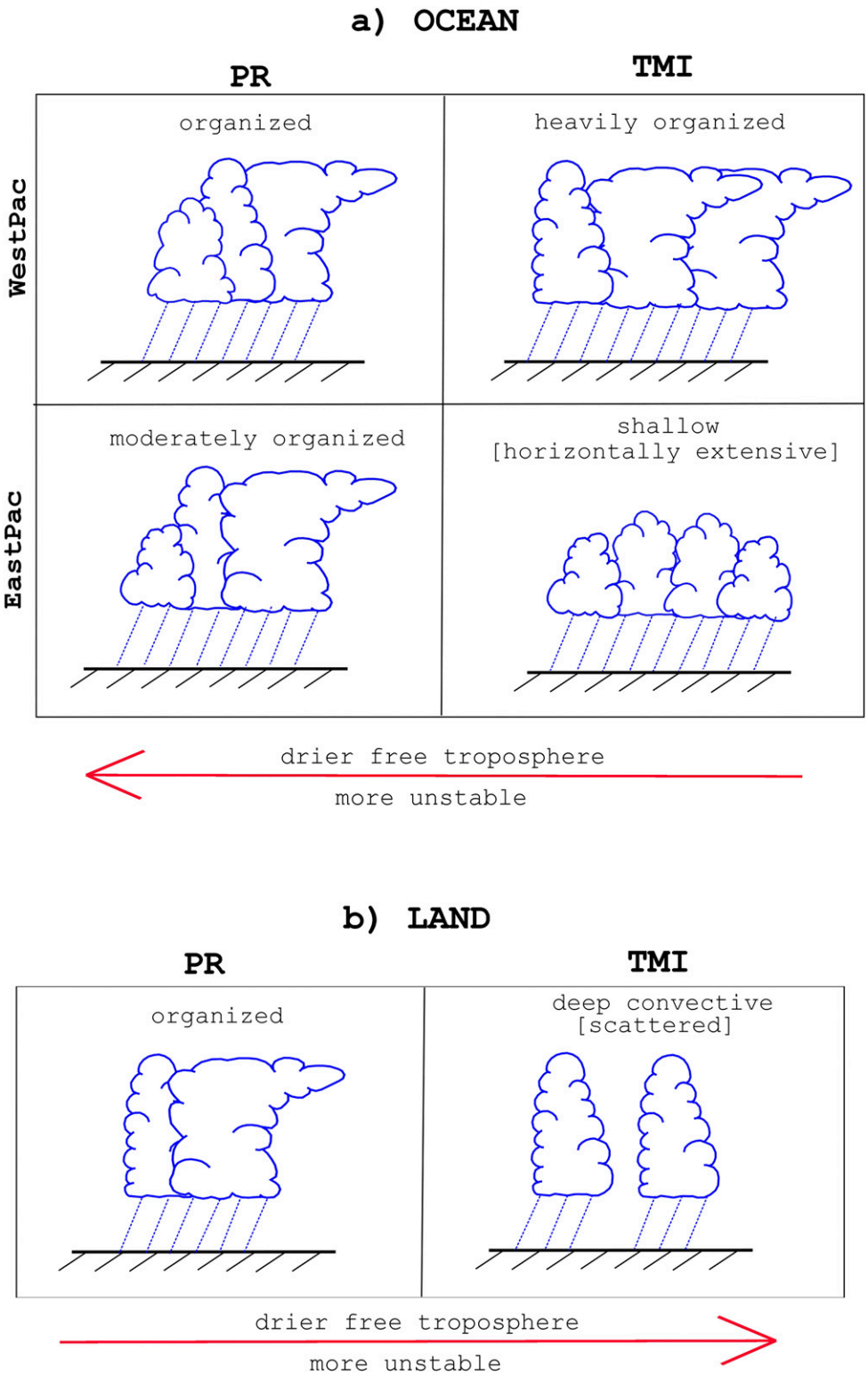

FIG. 13. Illustration of the PR–TMI differences when identifying heavy rainfall events as associated with organized precipitation. (a) The contrast between the eastern and western Pacific Oceans; (b) the differences over land.

Acknowledgments. This research is funded by Lembaga Pengelola Dana Pendidikan (LPDP), Ministry of Finance Republic of Indonesia, with the Contract PRJ-1875/LPDP/2014. The TRMM PR (2A12) and TMI (2A25) datasets analyzed in this work are available online from the NASA Precipitation Measurement Mission (PMM) archives (https://pmm.nasa.gov/data-access/downloads/TRMM). The *CloudSat* data are provided by http://cloudsat.atmos.colostate.edu/data. The ERA-Interim data are available at https://www.ecmwf.int/en/forecasts/datasets/reanalysis-datasets/ERA-Interim.

REFERENCES

Austin, R. T., A. J. Heymsfield, and G. L. Stephens, 2009: Retrieval of ice cloud microphysical parameters using the CloudSat millimeter-wave radar and temperature. *J. Geophys. Res.*, **114**, D00A23, https://doi.org/10.1029/2008JD010049.

Berg, W., T. L'Ecuyer, and C. Kummerow, 2006: Rainfall climate regimes: The relationship of regional TRMM rainfall biases to the environment. *J. Appl. Meteor. Climatol.*, **45**, 434–454, https://doi.org/10.1175/JAM2331.1.

Carr, N., and Coauthors, 2015: The influence of surface and precipitation characteristics on TRMM Microwave Imager rainfall retrieval uncertainty. *J. Hydrometeor.*, **16**, 1596–1614, https://doi.org/10.1175/JHM-D-14-0194.1.

CloudSat DPC, 2017: CloudSat 2B-GEOPROF. Accessed 22 February 2017, http://www.cloudsat.cira.colostate.edu/data-products/level-2b/2b-geoprof.

Dee, D. P., and Coauthors, 2011: The ERA-Interim reanalysis: Configuration and performance of the data assimilation system. *Quart. J. Roy. Meteor. Soc.*, **137**, 553–597, https://doi.org/10.1002/qj.828.

ECMWF, 2017: ERA Interim. Accessed 15 March 2017, https://www.ecmwf.int/en/forecasts/datasets/reanalysis-datasets/era-interim.

Furuzawa, F. A., and K. Nakamura, 2005: Differences of rainfall estimates over land by Tropical Rainfall Measuring Mission (TRMM) Precipitation Radar (PR) and TRMM Microwave Imager (TMI)—Dependence on storm height. *J. Appl. Meteor.*, **44**, 367–383, https://doi.org/10.1175/JAM-2200.1.

Gopalan, K., N.-Y. Wang, R. Ferraro, and C. Liu, 2010: Status of the TRMM 2A12 land precipitation algorithm. *J. Atmos. Oceanic Technol.*, **27**, 1343–1354, https://doi.org/10.1175/2010JTECHA1454.1.

Griffith, C. G., W. L. Woodley, P. G. Grube, D. W. Martin, J. Stout, and D. N. Sikdar, 1978: Rain estimation from geosynchronous satellite imagery—Visible and infrared studies. *Mon. Wea. Rev.*, **106**, 1153–1171, https://doi.org/10.1175/1520-0493(1978)106<1153:REFGSI>2.0.CO;2.

Hamada, A., Y. N. Takayabu, C. Liu, and E. J. Zipser, 2015: Weak linkage between the heaviest rainfall and tallest storms. *Nat. Commun.*, **6**, 6213, https://doi.org/10.1038/ncomms7213.

Henderson, D. S., C. D. Kummerow, D. A. Marks, and W. Berg, 2017: A regime-based evaluation of TRMM oceanic precipitation biases. *J. Atmos. Oceanic Technol.*, **34**, 2613–2635, https://doi.org/10.1175/JTECH-D-16-0244.1.

——, ——, and W. Berg, 2018: ENSO influence on TRMM tropical oceanic precipitation characteristics and rain rates. *J. Climate*, **31**, 3979–3998, https://doi.org/10.1175/JCLI-D-17-0276.1.

Heymsfield, A. J., A. Bansemer, P. R. Field, S. L. Durden, J. L. Stith, J. E. Dye, W. Hall, and C. A. Grainger, 2002: Observations and parameterizations of particle size distributions in deep tropical cirrus and stratiform precipitating clouds: Results from in situ observations in TRMM field campaigns. *J. Atmos. Sci.*, **59**, 3457–3491, https://doi.org/10.1175/1520-0469(2002)059<3457:OAPOPS>2.0.CO;2.

Hill, K. A., and G. M. Lackmann, 2009: Influence of environmental humidity on tropical cyclone size. *Mon. Wea. Rev.*, **137**, 3294–3315, https://doi.org/10.1175/2009MWR2679.1.

Igel, M. R., A. J. Drager, and S. C. Heever, 2014: A CloudSat cloud object partitioning technique and assessment and integration of deep convective anvil sensitivities to sea surface temperature. *J. Geophys. Res. Atmos.*, **119**, 10 515–10 535, https://doi.org/10.1002/2014JD021717.

Iguchi, T., T. Kozu, R. Meneghini, J. Awaka, and K. Okamoto, 2000: Rain-profiling algorithm for the TRMM precipitation radar. *J. Appl. Meteor.*, **39**, 2038–2052, https://doi.org/10.1175/1520-0450(2001)040<2038:RPAFTT>2.0.CO;2.

——, ——, J. Kwiatkowski, R. Meneghini, J. Awaka, and K. Okamoto, 2009: Uncertainties in the rain profiling algorithm for the TRMM precipitation radar. *J. Meteor. Soc. Japan*, **87A**, 1–30, https://doi.org/10.2151/jmsj.87A.1.

Kirstetter, P.-E., Y. Hong, J. J. Gourley, M. Schwaller, W. Petersen, and J. Zhang, 2013: Comparison of TRMM 2A25 products, version 6 and version 7, with NOAA/NSSL ground radar-based national mosaic QPE. *J. Hydrometeor.*, **14**, 661–669, https://doi.org/10.1175/JHM-D-12-030.1.

——, ——, J. Gourley, M. Schwaller, W. Petersen, and Q. Cao, 2015: Impact of sub-pixel rainfall variability on spaceborne precipitation estimation: Evaluating the TRMM 2A25 product. *Quart. J. Roy. Meteor. Soc.*, **141**, 953–966, https://doi.org/10.1002/qj.2416.

Kozu, T., T. Iguchi, T. Kubota, N. Yoshida, S. Seto, J. Kwiatkowski, and Y. N. Takayabu, 2009: Feasibility of raindrop size distribution parameter estimation with TRMM precipitation radar. *J. Meteor. Soc. Japan*, **87A**, 53–66, https://doi.org/10.2151/jmsj.87A.53.

Kummerow, C., 1998: Beamfilling errors in passive microwave rainfall retrievals. *J. Appl. Meteor.*, **37**, 356–370, https://doi.org/10.1175/1520-0450(1998)037<0356:BEIPMR>2.0.CO;2.

——, and L. Giglio, 1994: A passive microwave technique for estimating rainfall and vertical structure information from space. Part I: Algorithm description. *J. Appl. Meteor.*, **33**, 3–18, https://doi.org/10.1175/1520-0450(1994)033<0003:APMTFE>2.0.CO;2.

——, W. Barnes, T. Kozu, J. Shiue, and J. Simpson, 1998: The Tropical Rainfall Measuring Mission (TRMM) sensor package. *J. Atmos. Oceanic Technol.*, **15**, 809–817, https://doi.org/10.1175/1520-0426(1998)015<0809:TTRMMT>2.0.CO;2.

——, and Coauthors, 2001: The evolution of the Goddard Profiling Algorithm (GPROF) for rainfall estimation from passive microwave sensors. *J. Appl. Meteor.*, **40**, 1801–1820, https://doi.org/10.1175/1520-0450(2001)040<1801:TEOTGP>2.0.CO;2.

——, P. Poyner, W. Berg, and J. Thomas-Stahle, 2004: The effects of rainfall inhomogeneity on climate variability of rainfall estimated from passive microwave sensors. *J. Atmos. Oceanic Technol.*, **21**, 624–638, https://doi.org/10.1175/1520-0426(2004)021<0624:TEORIO>2.0.CO;2.

Liu, C., and E. J. Zipser, 2005: Global distribution of convection penetrating the tropical tropopause. *J. Geophys. Res.*, **110**, D23104, https://doi.org/10.1029/2005JD006063.

——, and ——, 2013: Regional variation of morphology of organized convection in the tropics and subtropics. *J. Geophys. Res. Atmos.*, **118**, 453–466, https://doi.org/10.1029/2012JD018409.

——, and ——, 2014: Differences between the surface precipitation estimates from the TRMM precipitation radar and passive microwave radiometer version 7 products. *J. Hydrometeor.*, **15**, 2157–2175, https://doi.org/10.1175/JHM-D-14-0051.1.

Lucas, C., E. J. Zipser, and B. S. Ferrier, 2000: Sensitivity of tropical west Pacific oceanic squall lines to tropospheric wind and moisture profiles. *J. Atmos. Sci.*, **57**, 2351–2373, https://doi.org/10.1175/1520-0469(2000)057<2351:SOTWPO>2.0.CO;2.

Masunaga, H., 2012: Short-term versus climatological relationship between precipitation and tropospheric humidity. *J. Climate*, **25**, 7983–7990, https://doi.org/10.1175/JCLI-D-12-00037.1.

——, T. Iguchi, R. Oki, and M. Kachi, 2002: Comparison of rainfall products derived from TRMM Microwave Imager and precipitation radar. *J. Appl. Meteor.*, **41**, 849–862, https://doi.org/10.1175/1520-0450(2002)041<0849:CORPDF>2.0.CO;2.

NASA, 2011a: Microwave brightness temperature (TMI). https://gcmd.nasa.gov/KeywordSearch/Metadata.do?Portal=daacs&KeywordPath=Parameters%7CSPECTRAL%2FENGINEERING%7CMICROWAVE%7CSENSOR+COUNTS&OrigMetadataNode=GCMD&EntryId=GES_DISC_TRMM_1B11_V7&MetadataView=Full&MetadataType=0&lbnode=mdlb2.

——, 2011b: TRMM Microwave imager (TMI) level 2A hydrometeor profile product. https://gcmd.nasa.gov/KeywordSearch/Metadata.do?Portal=NASA&KeywordPath=Parameters%7CATMOSPHERE%7CATMOSPHERIC+WATER+VAPOR%7CEVAPORATION&EntryId=GES_DISC_TRMM_2A12_V7&MetadataView=Full&MetadataType=0&lbnode=mdlb3.

——, 2011c: TRMM product level 2A precipitation radar (PR) rainfall rate and profile. https://gcmd.nasa.gov/KeywordSearch/Metadata.do?Portal=daacs&KeywordPath=Parameters%7CATMOSPHERE%7CPRECIPITATION%7CPRECIPITATION+ANOMALIES&EntryId=GES_DISC_TRMM_2A25_V7&MetadataView=Full&MetadataType=0&lbnode=mdlb1.

Nesbitt, S. W., R. Cifelli, and S. A. Rutledge, 2006: Storm morphology and rainfall characteristics of TRMM precipitation features. *Mon. Wea. Rev.*, **134**, 2702–2721, https://doi.org/10.1175/MWR3200.1.

Petković, V., and C. D. Kummerow, 2017: Understanding the sources of satellite passive microwave rainfall retrieval systematic errors over land. *J. Appl. Meteor. Climatol.*, **56**, 597–614, https://doi.org/10.1175/JAMC-D-16-0174.1.

Ramage, C. S., 1968: Role of a tropical "maritime continent" in the atmospheric circulation. *Mon. Wea. Rev.*, **96**, 365–370, https://doi.org/10.1175/1520-0493(1968)096<0365:ROATMC>2.0.CO;2.

Rasmussen, K. L., S. L. Choi, M. D. Zuluaga, and R. A. Houze, 2013: TRMM precipitation bias in extreme storms in South America. *Geophys. Res. Lett.*, **40**, 3457–3461, https://doi.org/10.1002/grl.50651.

Rickenbach, T. M., and S. A. Rutledge, 1998: Convection in TOGA COARE: Horizontal scale, morphology, and rainfall production. *J. Atmos. Sci.*, **55**, 2715–2729, https://doi.org/10.1175/1520-0469(1998)055<2715:CITCHS>2.0.CO;2.

Schumacher, C., and R. A. Houze Jr., 2000: Comparison of radar data from the TRMM satellite and Kwajalein oceanic validation site. *J. Appl. Meteor.*, **39**, 2151–2164, https://doi.org/10.1175/1520-0450(2001)040<2151:CORDFT>2.0.CO;2.

——, and ——, 2003: The TRMM precipitation radar's view of shallow, isolated rain. *J. Appl. Meteor.*, **42**, 1519–1524, https://doi.org/10.1175/1520-0450(2003)042<1519:TTPRVO>2.0.CO;2.

——, and ——, 2006: Stratiform precipitation production over sub-Saharan Africa and the tropical East Atlantic as observed by TRMM. *Quart. J. Roy. Meteor. Soc.*, **132**, 2235–2255, https://doi.org/10.1256/qj.05.121.

Sekaranom, A. B., and H. Masunaga, 2017: Comparison of TRMM-derived rainfall products for general and extreme rains over the Maritime Continent. *J. Appl. Meteor. Climatol.*, **56**, 1867–1881, https://doi.org/10.1175/JAMC-D-16-0272.1.

Sherwood, S. C., 1999: Convective precursors and predictability in the tropical western Pacific. *Mon. Wea. Rev.*, **127**, 2977–2991, https://doi.org/10.1175/1520-0493(1999)127<2977:CPAPIT>2.0.CO;2.

Shige, S., Y. N. Takayabu, W.-K. Tao, and D. E. Johnson, 2004: Spectral retrieval of latent heating profiles from TRMM PR data. Part I: Development of a model-based algorithm. *J. Appl. Meteor.*, **43**, 1095–1113, https://doi.org/10.1175/1520-0450(2004)043<1095:SROLHP>2.0.CO;2.

——, H. Sasaki, K. Okamoto, and T. Iguchi, 2006: Validation of rainfall estimates from the TRMM precipitation radar and microwave imager using a radiative transfer model: 1. Comparison of the version-5 and -6 products. *Geophys. Res. Lett.*, **33**, L13803, https://doi.org/10.1029/2006GL026350.

——, Y. N. Takayabu, and W.-K. Tao, 2008: Spectral retrieval of latent heating profiles from TRMM PR data. Part III: Estimating apparent moisture sink profiles over tropical oceans. *J. Appl. Meteor. Climatol.*, **47**, 620–640, https://doi.org/10.1175/2007JAMC1738.1.

Simpson, J., C. Kummerow, W.-K. Tao, and R. F. Adler, 1996: On the Tropical Rainfall Measuring Mission (TRMM). *Meteor. Atmos. Phys.*, **60**, 19–36, https://doi.org/10.1007/BF01029783.

Song, H.-J., and B.-J. Sohn, 2015: Two heavy rainfall types over the Korean peninsula in the humid East Asian summer environment: A satellite observation study. *Mon. Wea. Rev.*, **143**, 363–382, https://doi.org/10.1175/MWR-D-14-00184.1.

——, ——, S.-Y. Hong, and T. Hashino, 2017: Idealized numerical experiments on the microphysical evolution of warm-type heavy rainfall. *J. Geophys. Res. Atmos.*, **122**, 1685–1699, https://doi.org/10.1002/2016JD025637.

Stephens, G. L., and Coauthors, 2002: The CloudSat mission and the A-Train: A new dimension of space-based observations of clouds and precipitation. *Bull. Amer. Meteor. Soc.*, **83**, 1771–1790, https://doi.org/10.1175/BAMS-83-12-1771.

Tompkins, A. M., 2001: Organization of tropical convection in low vertical wind shears: The role of water vapor. *J. Atmos. Sci.*, **58**, 529–545, https://doi.org/10.1175/1520-0469(2001)058<0529:OOTCIL>2.0.CO;2.

Wang, N.-Y., C. Liu, R. Ferraro, D. Wolff, E. Zipser, and C. Kummerow, 2009: TRMM 2A12 land precipitation product—Status and future plans. *J. Meteor. Soc. Japan*, **87A**, 237–253, https://doi.org/10.2151/jmsj.87A.237.

Wilheit, T. T., 1986: Some comments on passive microwave measurement of rain. *Bull. Amer. Meteor. Soc.*, **67**, 1226–1232, https://doi.org/10.1175/1520-0477(1986)067<1226:SCOPMM>2.0.CO;2.

——, and Coauthors, 1994: Algorithms for the retrieval of rainfall from passive microwave measurements. *Remote Sens. Rev.*, **11**, 163–194, https://doi.org/10.1080/02757259409532264.

Yamamoto, M. K., F. A. Furuzawa, A. Higuchi, and K. Nakamura, 2008: Comparison of diurnal variations in precipitation systems observed by TRMM PR, TMI, and VIRS. *J. Climate*, **21**, 4011–4028, https://doi.org/10.1175/2007JCLI2079.1.

Zagrodnik, J. P., and H. Jiang, 2013: Investigation of PR and TMI version 6 and version 7 rainfall algorithms in landfalling tropical cyclones relative to the NEXRAD stage-IV Multisensor Precipitation Estimate dataset. *J. Appl. Meteor. Climatol.*, **52**, 2809–2827, https://doi.org/10.1175/JAMC-D-12-0274.1.